



# CHORUS

This is the accepted manuscript made available via CHORUS. The article has been published as:

## Potential-barrier effects in three-photon-ionization processes

Liang-Wen Pi and Anthony F. Starace

Phys. Rev. A **90**, 023403 — Published 4 August 2014

DOI: [10.1103/PhysRevA.90.023403](https://doi.org/10.1103/PhysRevA.90.023403)

# Potential Barrier Effects in Three-Photon Ionization Processes

Liang-Wen Pi and Anthony F. Starace

*Department of Physics and Astronomy, The University of Nebraska, Lincoln, NE 68588-0299*

Resonance-like enhancements of generalized three-photon cross sections for XUV ionization of Ar, Kr, and Xe are demonstrated and analyzed within a single-active-electron, central-potential model. The resonant-like behavior is shown to originate from the potential barriers experienced by intermediate- and final-state photoelectron wave packets corresponding to absorption of one, two, or three photons. The resonance-like profiles in the generalized three-photon ionization cross sections are shown to be similar to those found in the generalized two-photon ionization cross sections [Phys. Rev. A **82**, 053414 (2010)]. The complexity of Cooper minima in multiphoton ionization processes is also discussed. Owing to the similar resonance-like profiles found in both two- and three-photon generalized cross sections, we expect such potential barrier effects to be general features of multiphoton ionization processes in most atoms with occupied  $p$ - and  $d$ -subshells.

PACS numbers: 32.80.Aa, 32.80.Rm

## I. INTRODUCTION

Free-electron lasers (FELs) based upon self-amplified spontaneous emission (SASE) by relativistic electrons in magnetic undulators have enabled the experimental realization of intense, polarized, short pulses of tunable radiation extending from the extreme ultraviolet (EUV) to the hard X-ray regime (for recent reviews, see Refs. [1–3]). The Free-electron LASer in Hamburg (FLASH) [4–7] was soon followed by the SPring-8 Compact SASE Source (SCSS) in Japan [8], and the Linear Coherent Light Source (LCLS) at SLAC [9, 10]. Moreover, other FEL user facilities are being developed elsewhere (see, e.g., Refs. [11–13]). The high intensity of these novel FEL pulses has opened the way for experimental investigations of such nonlinear phenomena in the EUV and X-ray regimes as multiphoton ionization [14, 15], two-photon absorption [16], photon-photon elastic scattering [17], and second harmonic generation [18].

The advent of experimental nonlinear EUV and X-ray phenomena provides strong motivation for theory to obtain both qualitative and quantitative understanding of the new phenomena. A rather complete understanding exists for the linear process of atomic photoionization (see, e.g., the detailed analyses in Refs. [19–21]), but it remains to be determined to what extent that understanding applies to such nonlinear processes as multiphoton ionization. For atoms larger than He, a number of theoretical treatments of few-photon ionization processes including electron correlation effects have been carried out [22–38], primarily for valence shell electrons and for photon energies in the UV regime. However, in the EUV and X-ray regimes, multiphoton ionization of inner-shell electrons becomes possible and the number of allowed ionization channels becomes so large as to make *ab initio* treatment of all electron correlation effects difficult. For this reason, qualitative understanding of key features of multiphoton ionization in the EUV and X-ray regimes may prove useful for interpreting forthcoming experimental data on multiphoton ionization processes.

A main feature in many atomic photoionization spec-

tra is a resonance-like peak that occurs when an ionized electron absorbs sufficient energy from a photon to overcome an effective potential barrier (originating from a combination of the Coulomb potential due to the nucleus and all other atomic electrons and the centrifugal barrier due to the ionized electron’s orbital angular momentum) [19, 21]. These resonance-like peaks in atomic photoionization spectra have also been interpreted as originating from a collective (i.e., many-electron) oscillation of the atomic electrons [20, 39] in analogy to the well-known giant dipole resonance in nuclear physics. However, since such resonance-like peaks in the photoionization spectra for particular subshells do occur within a single-active electron model of an atom (which by definition does not include any electron correlations), the qualitative description of the phenomenon as a potential barrier effect is justified. Accurate treatment of electron correlations is necessary to describe the effects on other subshell spectra (via interchannel interactions) and to provide quantitatively accurate predictions [20, 21].

Another feature in many atomic photoionization spectra is a cross section minimum first observed experimentally by Ditchburn *et al.* [40] in alkali atoms. It was explained by Bates [41] and Seaton [42] as due to a change in sign of radial dipole matrix elements as a function of photon frequency. Later Cooper [43] extended the study of such cross section minima to rare gas atoms and closed-shell ions and formulated rules for their occurrence (see also the discussions in Sec. 4 of Ref. [19] and on pp. 55–58 of Ref. [21]). Owing to the formulation of these rules, based on results for a central potential model of the atom, the cross section minimum observed in the photoionization spectrum for some atoms is often called a “Cooper minimum.” Further studies of the systematics of zeros in radial dipole matrix elements have provided a general understanding of the occurrence of Cooper minima (CM) [44, 45]. Up to now however, CM have only been studied for single-photon ionization processes and their role in multiphoton ionization processes is unexplored.

We present in this paper single active electron approximation results for three-photon ionization of Ar, Kr,

and Xe atoms that demonstrate the occurrence of both resonance-like potential barrier effects and CM. We compare the present three-photon results with our prior two-photon results [46] to show their remarkable similarity when plotted on an appropriate energy scale. Our results provide a broader understanding of these resonance-like phenomena and suggest that potential barrier effects are general features of multiphoton ionization processes. We also demonstrate the greater complexity of CM phenomena in multiphoton ionization processes. Throughout this paper, we employ atomic units (a.u.,  $\hbar = e = m_e = 1$ ) unless otherwise indicated.

This paper is organized as follows. In Sec. II we describe briefly the theoretical methods used in our model potential calculations and demonstrate the accuracy of our numerical solutions. In Sec. III we present the frequency dependence of multiphoton ionization total and partial cross sections from particular subshells of Ar, Kr, and Xe for both three-photon and two-photon cases. Finally, in Sec. IV we summarize our results and present some conclusions.

## II. THEORETICAL CONSIDERATIONS AND APPROACH

The generalized  $N$ -photon ionization total cross section is [47]

$$\sigma_{(N)} = 2\pi(2\pi\alpha\omega)^N \sum_f \left| T_{f\leftarrow 0}^{(N)} \right|^2, \quad (1)$$

where  $T_{f\leftarrow 0}^{(N)}$  is the transition amplitude,  $\alpha$  is the fine structure constant, and  $\omega$  is the frequency of the laser field (assumed to be monochromatic and linearly-polarized). For the case  $N = 3$ , the three-photon transition amplitude from an initial state  $\Psi_0$  of energy  $E_0$  to a final state  $\Psi_3$  of energy  $E_3$  (where  $E_3 \equiv E_0 + 3\omega$ ) is

$$T_{f\leftarrow 0}^{(3)} = \sum_{i_1 i_2} \langle \Psi_3 | D | \Psi_{i_2} \rangle \frac{1}{E_0 + 2\omega - E_{i_2}} \times \langle \Psi_{i_2} | D | \Psi_{i_1} \rangle \frac{1}{E_0 + \omega - E_{i_1}} \langle \Psi_{i_1} | D | \Psi_0 \rangle, \quad (2)$$

where the interaction of the laser field with the atom is treated using lowest-order perturbation theory,  $D$  is the electric dipole operator, and  $\Psi_{i_1, i_2}$  of energy  $E_{i_1, i_2}$  are the first and second intermediate states. Using the same notations, the two-photon transition amplitude from an initial state  $\Psi_0$  of energy  $E_0$  to a final state  $\Psi_2$  of energy  $E_2$  ( $E_2 \equiv E_0 + 2\omega$ ) is

$$T_{f\leftarrow 0}^{(2)} = \sum_{i_1} \langle \Psi_2 | D | \Psi_{i_1} \rangle \frac{1}{E_0 + \omega - E_{i_1}} \langle \Psi_{i_1} | D | \Psi_0 \rangle. \quad (3)$$

In order to avoid the explicit summations over intermediate states, we evaluate Eqs. (2) and (3) using the

Dalgarno-Lewis method [48]. Briefly, one defines the following two intermediate-state wave packets:

$$|\Lambda_1\rangle \equiv \sum_{i_1} |\Psi_{i_1}\rangle \frac{1}{E_0 + \omega - E_{i_1}} \langle \Psi_{i_1} | D | \Psi_0 \rangle, \quad (4a)$$

$$|\Lambda_2\rangle \equiv \sum_{i_2} |\Psi_{i_2}\rangle \frac{1}{E_0 + 2\omega - E_{i_2}} \langle \Psi_{i_2} | D | \Lambda_1 \rangle. \quad (4b)$$

These wave-packet states are the solutions of the following two coupled, inhomogeneous Schrödinger equations:

$$(E_0 + \omega - H)|\Lambda_1\rangle = D|\Psi_0\rangle, \quad (5a)$$

$$(E_0 + 2\omega - H)|\Lambda_2\rangle = D|\Lambda_1\rangle, \quad (5b)$$

where  $H$  is the  $n$ -electron, non-relativistic model Hamiltonian,

$$H = \sum_{j=1}^n \left[ -\frac{1}{2} \nabla_j^2 + V_{HS}(r_j) \right], \quad (6)$$

where  $V_{HS}(r_j)$  is the Herman-Skillman central potential [49]. Solution of the coupled equations in (5) sequentially to obtain the states  $\Lambda_N$  (for  $N=1, 2$ ) then allows one to calculate the transition amplitudes in Eqs. (2) and (3) as

$$T_{f\leftarrow 0}^{(2)} \equiv \langle \Psi_2 | D | \Lambda_1 \rangle, \quad (7a)$$

$$T_{f\leftarrow 0}^{(3)} \equiv \langle \Psi_3 | D | \Lambda_2 \rangle. \quad (7b)$$

In the single-active-electron approximation, the angular and radial variables of both the eigenstates  $\Psi_N$  and the intermediate states  $\Lambda_N$  can be separated. One can thus write the radial parts of the equations in (5) as [50]

$$(\varepsilon_0 + \omega - h_{l_1})|\lambda_{\varepsilon_1 l_1}\rangle = -\frac{1}{2}r|\psi_{n_0 l_0}\rangle, \quad (8a)$$

$$(\varepsilon_0 + 2\omega - h_{l_2})|\lambda_{\varepsilon_2 l_2}\rangle = -\frac{1}{2}r|\lambda_{\varepsilon_1 l_1}\rangle, \quad (8b)$$

where  $\varepsilon_N$  ( $\equiv \varepsilon_0 + N\omega$ ) and  $l_N$  are the energy and orbital angular momentum of the single active electron, where  $\varepsilon_0$  is the energy of its initial state  $\psi_{n_0 l_0}$ . Each of the radial Hamiltonians  $h_l$  in Eq. (8) for the single active electron is given by:

$$h_l = -\frac{1}{2}d^2/dr^2 + V_{HS}(r) + l(l+1)/2r^2. \quad (9)$$

The transition amplitudes in (7) can be rewritten as summations over products of angular factors and radial integrals:

$$T_{f\leftarrow 0}^{(2)} = \sum_{L_1 l_1} A_2(L_1, l_1) \langle \psi_{\varepsilon_2 l_2} | r | \lambda_{\varepsilon_1 l_1} \rangle, \quad (10a)$$

$$T_{f\leftarrow 0}^{(3)} = \sum_{L_2 l_2} \sum_{L_1 l_1} A_3(L_2, l_2; L_1, l_1) \langle \psi_{\varepsilon_3 l_3} | r | \lambda_{\varepsilon_2 l_2} \rangle, \quad (10b)$$

where  $L_N$  is the total orbital angular momentum of the atomic system following absorption of  $N$  photons.

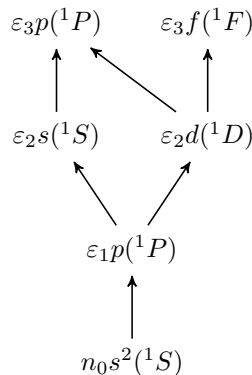


FIG. 1. Schematic diagram of all one-, two- and three-photon ionization channels allowed by electric dipole selection rules for ionization from an  $s$ -subshell of a closed-shell atom. For simplicity, we use here the notation  $\varepsilon_N l_N(^1 L_N)$  as a short designation for the state  $n_0 l_0^{2l_0+1} \varepsilon_N l_N(^1 L_N)$  (where  $l_0 = 0$  in this case and  $N$  indicates the number of photons absorbed), i.e., the ionic core configuration  $n_0 s^1(^2 S)$  is suppressed for all excited and ionized states. Note that for each final state, there may be more than one contributing channels that interfere coherently.

The radial function of the  $N$ th intermediate state,  $\lambda_{\varepsilon_N l_N}(r)$ , satisfies different boundary conditions depending on the value of  $\varepsilon_N$ . For  $\varepsilon_N < 0$ ,  $\lambda_{\varepsilon_N l_N}(r)$  is a real function and goes to zero when  $r$  goes to infinity; for  $\varepsilon_N > 0$ ,  $\lambda_{\varepsilon_N l_N}(r)$  is a complex function and satisfies outgoing-wave boundary conditions [33, 50, 51]. Taking into account these boundary conditions, Eq. (8) may be solved numerically using Runge-Kutta methods to obtain  $\lambda_{\varepsilon_N l_N}$ . The evaluation of the radial integrals  $\langle \psi_{\varepsilon_N' l_N'} | r | \lambda_{\varepsilon_N l_N} \rangle$  in Eq. (10) is then straightforward. In the above-threshold-ionization case (i.e.,  $\varepsilon_N > 0$ ), the free-free dipole matrix elements appearing in Eq. (10) are evaluated using a complex coordinate rotation method [52]. The angular factors,  $A_2$  and  $A_3$ , of the electric dipole transition amplitudes in Eq. (10) are evaluated using graphical angular momentum methods (see, e.g., Refs [53–55]); the results are given in the Appendix. We only consider multiphoton ionization of closed-shell atoms for the case of a linearly-polarized laser field, which greatly simplifies the expressions for the angular momentum factors,  $A_2$  and  $A_3$ , owing to the zero total angular momentum of the initial state.

Schematic diagrams of all one-, two-, and three-photon ionization channels allowed by electric dipole selection rules are shown in Figs. 1, 2, and 3 respectively for  $s^2(^1 S)$ ,  $p^6(^1 S)$ , and  $d^{10}(^1 S)$  initial closed subshells. The state of the single active electron after absorbing  $N$  photons is indicated by its energy,  $\varepsilon_N$ , and orbital angular momentum,  $l_N$  (where  $s$ ,  $p$ , and  $d$  indicate respectively  $l_N = 0, 1$ , and  $2$ ); the total spin and orbital angular momentum of the active electron and the singly-ionized core are given in parentheses,  $(^1 L)$ , i.e., the notation  $\varepsilon_N l_N(^1 L_N)$  in Figs. 1 – 3 stands for the final state of the following

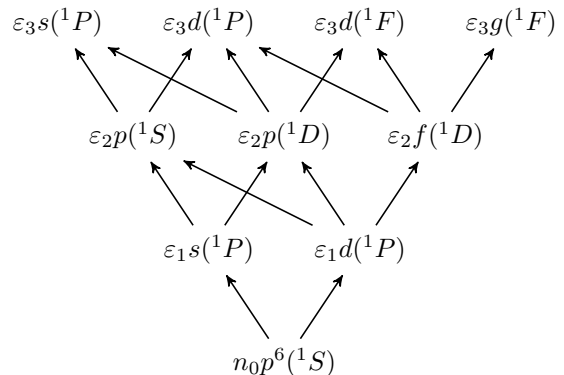


FIG. 2. Same as Fig. 1 but for ionization from a  $p$ -subshell of a closed-shell atom. The ionic core configuration  $n_0 p^5(^2 P)$  is suppressed for all excited and ionized states.

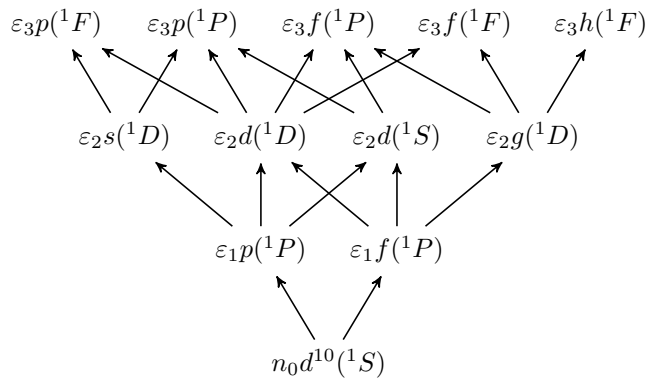


FIG. 3. Same as Fig. 1 but for ionization from a  $d$ -subshell of a closed-shell atom. The ionic core configuration  $n_0 d^9(^2 D)$  is suppressed for all excited and ionized states.

process:

$$n_0 l_0^{2l_0+2}(^1 S) + N\gamma \rightarrow n_0 l_0^{2l_0+1} \varepsilon_N l_N(^1 L_N). \quad (11)$$

Each arrow in Figs. 1 – 3 represents the absorption of a photon. Notice that those states labeled with  $\varepsilon_2$  are the final states of two-photon ionization processes. The partial cross sections of all final states (labeled with  $\varepsilon_2$  and  $\varepsilon_3$  for two- and three-photon ionization) are summed to get the total cross sections in Eq. (1). Each final state may have contributions from more than one channel; as indicated in Eq. (10), these contributions are summed coherently.

Figure 4 shows the effective radial potentials,  $V_{eff}^l(r) = V_{HS}(r) + l(l+1)/2r^2$ , for Ar ( $l = 2$ ), Kr ( $l = 2$ ), and Xe ( $l = 3$ ). Notice that for certain ranges of the radial coordinate,  $r$ , these three potentials form barriers with different barrier heights. Many atoms have effective potential barriers for electrons with  $l = 2$  or  $3$  (cf. Fig. 17 in [19]). But for pure Coulomb potentials, as for the H atom,  $V_{eff}^l(r)$  never has a barrier. When an intermediate- or final-state of the photoelectron has an orbital angular momentum for which the effective po-

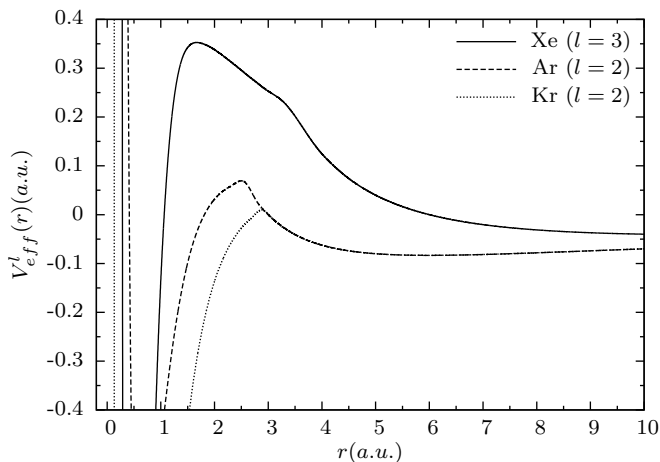


FIG. 4. Effective radial potentials,  $V_{eff}^l(r) \equiv l(l+1)/2r^2 + V_{HS}(r)$ , for electrons having orbital angular momentum  $l = 2$  in Ar and Kr and  $l = 3$  in Xe.

tential has a potential barrier, the energy-dependence of the transition amplitude (and hence of the total cross section) may exhibit resonance-like behavior. This is because for intermediate- or final-state photoelectron energies below the potential barrier, the corresponding radial wave functions for these states are located predominantly in the outer potential well. As the energies of these states approach the top of the barrier, however, their radial wave functions move in to the inner well region, resulting in a strong overlap with the initial state radial wave function of the photoelectron (cf. Fig. 5 on p.49 of Ref. [21]). As the energy of the wave packet increases above the top of the barrier, the oscillations of its radial part increase, resulting in cancellations that reduce the transition amplitude from the initial bound state. In brief, ionization from a bound state located in the inner well becomes maximal when an intermediate- or final-state wave packet migrates from the outer well to the inner well as its energy approaches the vicinity of the barrier height.

From the above discussion it is clear that the key energy variable for the active electron (in either an intermediate state wave packet or in the final state) is its energy relative to the ionization threshold just below an effective potential barrier. Since the active electron, initially in the  $n_0l_0$ -subshell with energy  $\varepsilon_{n_0l_0}$ , may probe the barrier after absorbing  $N$  photons, this key energy may be defined as  $\varepsilon_N \equiv \varepsilon_{n_0l_0} + N\omega$ . For convenience in converting the energies  $\varepsilon_N$  (used in presenting our results in Sec. III) to photon energies, we present in Table I the binding energies ( $\equiv -\varepsilon_{n_0l_0}$ ) of the various atomic  $n_0l_0$ -subshells considered in Sec. III. Our results for these binding energies agree very well with those in Ref. [49].

In order to confirm the accuracy of our numerical calculations, we have calculated the generalized three-photon cross sections for ionization of the ground state of atomic hydrogen and compared our results with those of others [56–58]. Table II shows the comparisons. Agree-

TABLE I. The binding energies (in a.u.) of different atomic  $n_0l_0$ -subshells calculated using the Herman-Skillman model potential [49]. The first column gives the target atoms and the first row indicates the  $n_0l_0$ -subshells.

atom	2s	2p	3s	3p	3d	4s	4d
Ar	11.43	9.10	1.05	0.533			
Kr	67.77	61.63	9.87	7.63			
Xe			38.48	33.95	25.48	7.09	2.63

ment up to three significant figures can be seen for a wide range of laser photon energies. The only exceptions are for the three wavelengths 102.5, 102.6 and 121.52 nm, which correspond to photon energies approaching resonance with an intermediate state. For energies in the vicinity of such resonances, the ionization cross sections are extremely sensitive to the photon energy used in the numerical calculations; also in our calculations the energy widths of the resonance states are not included.

### III. RESULTS AND DISCUSSION

In this section we present results that demonstrate potential barrier effects in the generalized three-photon ionization cross sections for particular subshells of Ar, Kr, and Xe atoms. These effects are shown to appear whenever the final or intermediate state wave packet of the active electron probes the top of a potential barrier. We also compare these features in three-photon ionization spectra with similar ones in the generalized two-photon ionization cross sections. Moreover, we demonstrate evidence for CM in the vicinity of these resonance-like features in the generalized multiphoton cross sections.

The occurrence of resonance-like potential barrier effects in multiphoton ionization spectra requires that the active electron has both appropriate orbital angular momentum and appropriate energy. Its orbital angular momentum must generally have the values  $l = 2, 3$ . Also, the atomic system must have an effective potential that has a potential barrier for these values of electron orbital angular momentum, e.g., as for the rare gas atoms whose effective potentials for  $l = 2, 3$  are shown in Fig. 4. Moreover, the energy of the intermediate or final state of the electron must be such that it probes the top of the effective potential barrier. Since most such barrier heights are in the energy range  $0 \leq \varepsilon_N \leq 0.5$ , the resonance-like features generally occur close to the ionization threshold for the corresponding intermediate or final state single-active-electron channels. In what follows, we present our results in order of the single-active-electron energies  $\varepsilon_N$  that probe an effective potential barrier, beginning with  $N = 1$ , corresponding to the intermediate state electron wave packet after absorption of the first photon, continuing with  $N = 2$ , corresponding to the intermediate state electron wave packet after absorption of two photons, and ending with  $N = 3$ , corresponding to the final state of

TABLE II. The generalized three-photon ionization cross section  $\sigma_{(3)}$  ( $\text{cm}^6 \text{s}^2$ ) of H(1s) for linearly polarized light.  $\lambda$  is the wavelength of the laser field and  $\omega$  is the photon energy. The integers  $n$  in parentheses denote the following:  $(-n) \equiv 10^{-n}$ .

$\lambda(\text{nm})$	$\omega(\text{a.u.})$	Previous works	Present
10	4.556	7.73(-93) <sup>a</sup>	7.71(-93)
20	2.278	1.15(-90) <sup>a</sup>	1.16(-90)
30	1.519	2.10(-89) <sup>a</sup>	2.09(-89)
40	1.139	1.64(-88) <sup>a</sup>	1.63(-88)
50	0.911	8.00(-88) <sup>a</sup>	8.03(-88)
60	0.759	2.92(-87) <sup>a</sup>	2.93(-87)
70	0.651	8.77(-87) <sup>a</sup>	8.72(-87)
80	0.570	2.28(-86) <sup>a</sup>	2.29(-86)
90	0.506	5.34(-86) <sup>a</sup>	5.38(-86)
97.2	0.4690	1.80(-83) <sup>b</sup>	1.80(-83)
97.3	0.4685	2.81(-83) <sup>b</sup>	2.82(-83)
99.5	0.458	5.60(-86) <sup>b</sup>	5.61(-86)
102.5	0.4448	3.32(-82) <sup>b</sup>	1.06(-82)
102.6	0.4443	2.75(-82) <sup>b</sup>	8.38(-82)
109	0.418	1.10(-85) <sup>b</sup>	1.10(-85)
120	0.380	1.52(-83) <sup>b</sup>	1.52(-83)
121.52	0.3751	4.15(-80) <sup>b</sup>	2.11(-80)
121.6	0.3749	5.04(-80) <sup>b</sup>	5.05(-80)
122	0.3737	2.89(-82) <sup>b</sup>	2.90(-82)
126	0.362	5.43(-84) <sup>b</sup>	5.43(-84)
140	0.326	2.02(-84) <sup>b</sup>	2.03(-84)
150	0.304	2.36(-84) <sup>b</sup>	2.37(-84)
160	0.285	3.12(-84) <sup>b</sup>	3.11(-84)
170	0.268	4.22(-84) <sup>b</sup>	4.23(-84)
180	0.253	5.78(-84) <sup>b</sup>	5.78(-84)
190	0.240	1.28(-82) <sup>c</sup>	1.28(-82)
200	0.228	5.36(-84) <sup>c</sup>	5.35(-84)
210	0.217	2.27(-83) <sup>c</sup>	2.27(-83)
220	0.207	1.30(-83) <sup>c</sup>	1.30(-83)
230	0.198	1.97(-83) <sup>c</sup>	1.97(-83)
240	0.190	4.83(-82) <sup>c</sup>	4.83(-82)
250	0.182	1.86(-82) <sup>c</sup>	1.86(-82)
260	0.175	5.85(-83) <sup>c</sup>	5.85(-83)

<sup>a</sup> Results of Karule and Gailitis [58] for  $\omega > 0.5$ , the ionization threshold.

<sup>b</sup> Results of Karule [56] for  $0.5 > \omega > 0.25$ .

<sup>c</sup> Results of Gao and Starace [57] for  $0.25 > \omega > 0.5/3$ .

the electron after absorbing three photons.

### A. First Intermediate State Potential Barrier Effects

We define the first intermediate state as the virtual intermediate-state wave packet  $|\Lambda_1\rangle$  [cf. Eqs. (4a) and (5a)] of the photoelectron after absorbing one photon from its initial subshell. The photon energies we consider here are above the one-photon ionization thresholds for the  $n_0l_0$ -subshells considered. First we consider the two- and three-photon ionization of the 3d- and 4d-subshells of Xe. Figs. 5(a) and 5(b) show the generalized three-photon total cross sections for ionization of

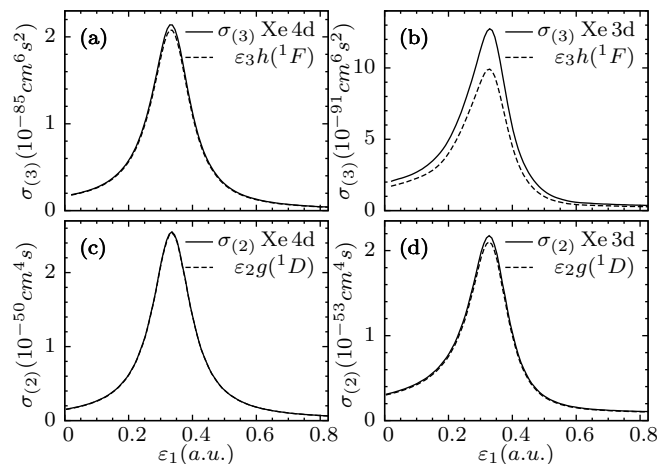


FIG. 5. *Top panels:* Generalized total cross sections  $\sigma_{(3)}$  (solid lines) for three-photon ionization of (a) the Xe 4d-subshell and (b) the Xe 3d-subshell; in each panel dashed lines show the partial cross section for the  $\varepsilon_3 h(^1F)$  channel. *Bottom panels:* Generalized total cross sections  $\sigma_{(2)}$  (solid lines) for two-photon ionization of (c) the Xe 4d-subshell and (d) the Xe 3d-subshell; in each panel dashed lines show the partial cross section for the  $\varepsilon_2 g(^1D)$  channel. All panels are plotted vs.  $\varepsilon_1 \equiv \varepsilon_{nd} + \omega$ , where  $\varepsilon_{nd}$  is the  $nd$ -orbital energy.

the Xe 4d- and 3d-subshells, respectively, plotted vs. the energy  $\varepsilon_1 \equiv \varepsilon_{nd} + \omega$  of the radial part of the photoelectron's intermediate state wave packet,  $\lambda_{\varepsilon_1 l_1}(r)$ . Figs. 5(c) and 5(d) show the generalized two-photon total cross sections for ionization of the Xe 4d- and 3d-subshells, respectively, plotted vs. the energy  $\varepsilon_1$ . Note that when plotting the results for different subshells over the same range of values of  $\varepsilon_1$ , the corresponding photon energies  $\omega$  are different owing to the different binding energies of the Xe 3d- and 4d-subshells. Although the total cross sections (solid lines) are for ionization by different numbers of photons from different subshells, the resonance-like shapes in the four panels of Fig. 5 are remarkably similar: Each exhibits a smooth, broad peak centered at about  $\varepsilon_1 = 0.34 \text{ a.u.}$ , which is very close to the Xe ( $l = 3$ ) potential barrier height,  $0.35 \text{ a.u.}$ , shown in Fig. 4. A reasonable explanation of this similarity is that the shape of this giant resonance is determined by the Xe ( $l = 3$ ) potential barrier (cf. Fig. 4), which is the same for all four cases in Fig. 5. Moreover, our calculations show that in each case there is a dominant final-state channel (indicated by dashed lines): the  $\varepsilon_3 h(^1F)$  channel in the case of three-photon ionization and the  $\varepsilon_2 g(^1D)$  channel in the case of two-photon ionization. As shown in Fig. 3, both channels involve the dipole transition  $\varepsilon_0 d^{10}(^1S) \rightarrow \varepsilon_1 f(^1P)$  when the first photon is absorbed, and  $\varepsilon_1 f(^1P)$  is the first intermediate state which probes the potential barrier and generates the giant resonance shape in the total cross section. If we take a close look of the dominant final-state channel  $\varepsilon_3 h(^1F)$ , there is a sequence of transitions in which both the photoelectron's orbital angular momentum and the system's total an-

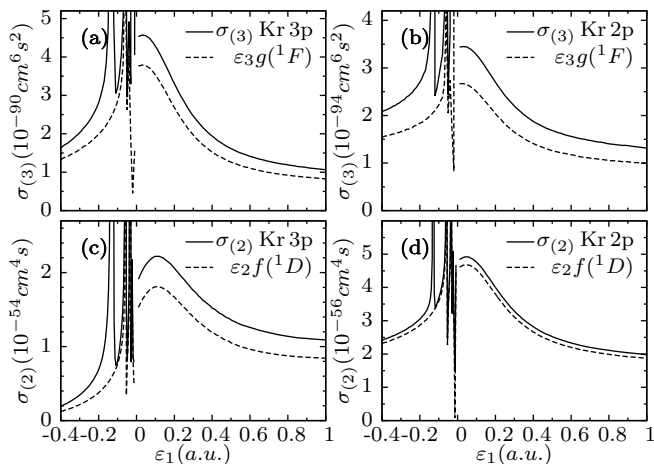


FIG. 6. *Top panels:* Generalized total cross sections  $\sigma_{(3)}$  (solid lines) for three-photon ionization of (a) the Kr 3p-subshell and (b) the Kr 2p-subshell; in each panel dashed lines show the partial cross section for the  $\varepsilon_3 g(^1F)$  channel. *Bottom panels:* Generalized total cross sections  $\sigma_{(2)}$  (solid lines) for two-photon ionization of (c) the Kr 3p-subshell and (d) the Kr 2p-subshell; in each panel dashed lines show the partial cross section for the  $\varepsilon_2 f(^1D)$  channel. All panels are plotted vs.  $\varepsilon_1 \equiv \varepsilon_{np} + \omega$ , where  $\varepsilon_{np}$  is the  $np$ -orbital energy.

gular momentum increase with each photon absorption, i.e.,  $\varepsilon_0 d^{10}(^1S) \rightarrow \varepsilon_1 f(^1P) \rightarrow \varepsilon_2 g(^1D) \rightarrow \varepsilon_3 h(^1F)$ . Classically, this is the preferred sequence of channels. All other final channels also have contributions from the first intermediate  $\varepsilon_1 f(^1P)$  state that experiences the potential barrier, but their contributions are much smaller. Similar reasoning is applicable for the final-state channel  $\varepsilon_2 g(^1D)$  in the case of two-photon ionization. The Xe 4d-subshell giant resonance in the case of two-photon ionization has been analyzed in detail in Ref. [46].

The generality of potential barrier effects is demonstrated in Figs. 6 and 7, in which we compare the generalized two- and three-photon cross sections for ionization from the 2p and 3p subshells of Kr and Ar, respectively, plotted vs. the energy  $\varepsilon_1 \equiv \varepsilon_{np} + \omega$  of the photoelectron's first intermediate state. The shapes of the resonance-like features in these generalized multiphoton ionization cross sections from  $np$ -subshells are qualitatively similar to those in Fig. 5 discussed above, but with two differences: First, they all have Rydberg resonances below  $\varepsilon_1 = 0$ . Second, the broad resonance extends into the below threshold energy region (i.e.,  $\varepsilon_1 < 0$ ) owing to the low heights of the  $l = 2$  potential barriers for Kr and Ar (cf. Fig. 4), so that the resonance-like maximum occurs close to  $\varepsilon_1 = 0$ . Our calculations show that there is a dominant final-state channel (indicated by the dashed lines) in each case: the  $\varepsilon_3 g(^1F)$  channel in the case of three-photon ionization and the  $\varepsilon_2 f(^1D)$  channel in the case of two-photon ionization. As shown in Fig. 2, both of these channels involve the dipole transition  $\varepsilon_0 p^6(^1S) \rightarrow \varepsilon_1 d(^1P)$  when the first photon is absorbed, and  $\varepsilon_1 d(^1P)$  is the first intermediate state which probes

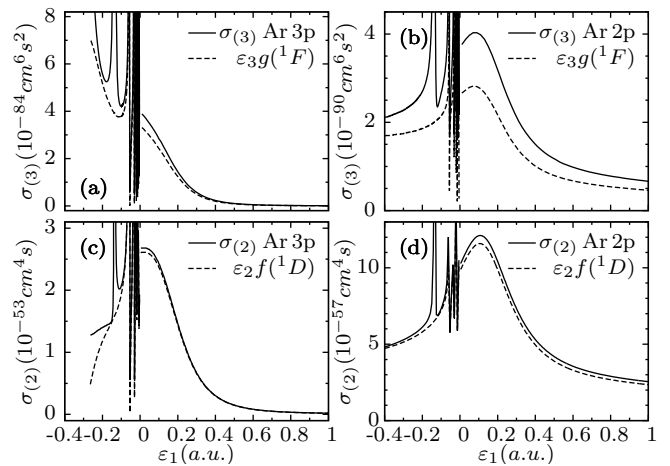


FIG. 7. *Top panels:* Generalized total cross sections  $\sigma_{(3)}$  (solid lines) for three-photon ionization of (a) the Ar 3p-subshell and (b) the Ar 2p-subshell; in each panel dashed lines show the partial cross section for the  $\varepsilon_3 g(^1F)$  channel. *Bottom panels:* Generalized total cross sections  $\sigma_{(2)}$  (solid lines) for two-photon ionization of (c) the Ar 3p-subshell and (d) the Ar 2p-subshell; in each panel dashed lines show the partial cross section for the  $\varepsilon_2 f(^1D)$  channel. All panels are plotted vs.  $\varepsilon_1 \equiv \varepsilon_{np} + \omega$ , where  $\varepsilon_{np}$  is the  $np$ -orbital energy.

the  $l = 2$  potential barrier and generates the resonance-like shapes in the total multiphoton cross sections.

Comparing the resonance-like features originating from the potential barriers probed by the first intermediate state photoelectron wave packet in both two- and three-photon ionization, and it is clear that the total multiphoton cross sections for the 2p- and 3p-subshells of Kr and Ar are more similar to each other than to those for the 3d- and 4d-subshells of Xe. Clearly the differences stem from the fact that the former originate from the  $l = 2$  potential barriers in Kr and Ar, while the latter originate from the  $l = 3$  potential barrier in the case of Xe. Nevertheless, the qualitative shapes and the energy locations of the resonance-like features appears to be independent of the number of photons and the binding energy of the initial subshell that is ionized; rather, these features all relate to the shapes of the potential barriers shown in Fig. 4. The  $l = 3$  potential barrier in the case of Xe is broader and higher than are the  $l = 2$  potential barriers in the cases of Kr and Ar, which leads to narrower resonance-like shapes in the generalized multiphoton ionization cross sections for Xe that are located at higher energies above the threshold for  $\varepsilon_1$ .

## B. Second Intermediate State Potential Barrier Effects

We define the second intermediate state in three-photon ionization as the virtual intermediate-state wave packet  $|\Lambda_2\rangle$  [cf. Eqs. (4b) and (5b)] of the photoelectron after absorbing two photons from its initial sub-

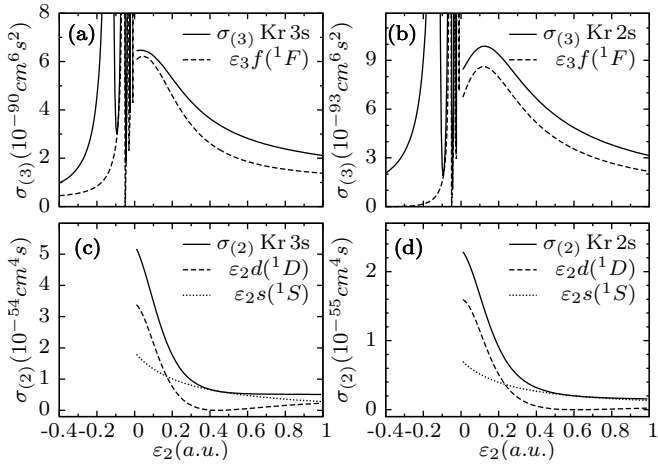


FIG. 8. *Top panels:* Generalized total cross sections  $\sigma_{(3)}$  (solid lines) for three-photon ionization of (a) the Kr 3s-subshell and (b) the Kr 2s-subshell; in each panel dashed lines show the partial cross section for the  $\varepsilon_3 f(^1F)$  channel. *Bottom panels:* Generalized total cross sections  $\sigma_{(2)}$  (solid lines) for two-photon ionization of (c) the Kr 3s-subshell and (d) the Kr 2s-subshell; in each panel dashed lines and dotted lines show the partial cross sections for the  $\varepsilon_2 d(^1D)$  and  $\varepsilon_2 s(^1S)$  channels respectively. All panels are plotted vs.  $\varepsilon_2 \equiv \varepsilon_{ns} + 2\omega$ , where  $\varepsilon_{ns}$  is the  $ns$ -orbital energy.

shell (cf. those states with energy  $\varepsilon_2$  in Figs. 1, 2, and 3). The photon energies we consider here are above the two-photon ionization thresholds for the  $n_0 l_0$ -subshells considered. The second state in two-photon ionization is the final state. In both two- and three-photon ionization processes these second states have the same angular momenta; however, the radial parts of the states in two- and three-photon ionization satisfy different boundary conditions. For two-photon ionization processes, the final state  $\psi_{\varepsilon_2 l_2}(r)$  satisfies the homogeneous Schrödinger equation with incoming-wave boundary conditions. For three-photon ionization processes, the second intermediate state  $\lambda_{\varepsilon_2 l_2}(r)$  satisfies the inhomogeneous Schrödinger Eq. (5b) with outgoing-wave boundary conditions [33, 50, 51]. Most noticeable is the fact that for two-photon ionization, the generalized cross section only exists for  $\varepsilon_2 \geq 0$  whereas for three-photon ionization, the generalized cross section extends above and below  $\varepsilon_2 = 0$ .

In Figs. 8(a) and 8(b) we present the generalized three-photon ionization cross sections from the Kr 3s- and 2s-subshells respectively. There is a remarkable similarity between the shapes of these generalized cross sections and those for three-photon ionization of the Kr 3p- and 2p-subshells shown respectively in Figs. 6(a) and 6(b). The reason for these similarities is that each of these ionization processes involves the dipole transition  $p \rightarrow d$  that probes the  $l = 2$  potential barrier in Kr (cf. Fig. 4). In Fig. 8 the active electron from an initial  $s$ -subshell probes the  $l = 2$  potential barrier after absorbing two photons; in Fig. 6 the active electron from an initial  $p$ -

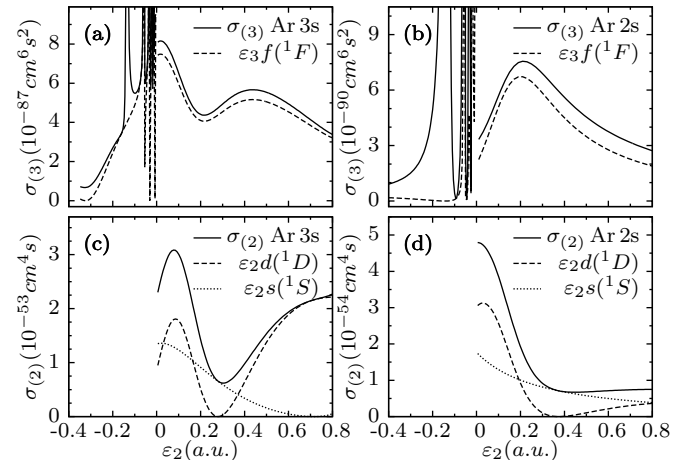


FIG. 9. *Top panels:* Generalized total cross sections  $\sigma_{(3)}$  (solid lines) for three-photon ionization of (a) the Ar 3s-subshell and (b) the Ar 2s-subshell; in each panel dashed lines show the partial cross section for the  $\varepsilon_3 f(^1F)$  channel. *Bottom panels:* Generalized total cross sections  $\sigma_{(2)}$  (solid lines) for two-photon ionization of (c) the Ar 3s-subshell and (d) the Ar 2s-subshell; in each panel dashed lines and dotted lines show the partial cross sections for the  $\varepsilon_2 d(^1D)$  and  $\varepsilon_2 s(^1S)$  channels respectively. All panels are plotted vs.  $\varepsilon_2 \equiv \varepsilon_{ns} + 2\omega$ , where  $\varepsilon_{ns}$  is the  $ns$ -orbital energy.

subshell probes this barrier after absorbing one photon.

In Figs. 8(c) and 8(d) we present the generalized two-photon ionization cross sections from the Kr 3s- and 2s-subshells. The shapes of these cross sections differ from those for the corresponding three-photon ionization cross sections simply because  $\varepsilon_2 \geq 0$  for a two-photon ionization process. From Fig. 1 we see that two channels contribute to the total generalized two-photon ionization cross sections leading to the final states  $\varepsilon_2 d(^1D)$  and  $\varepsilon_2 s(^1S)$ . As expected, near threshold the channel leading to the  $\varepsilon_2 d(^1D)$  final state dominates since only that one involves the  $p \rightarrow d$  dipole transition that probes the  $l = 2$  potential barrier.

In Fig. 9 we present the generalized three- and two-photon ionization cross sections from the Ar 3s- and 2s-subshells. The results are qualitatively similar to those from the same subshells of Kr that are shown in Fig. 8, with the exception of the minima in the cross sections from the Ar 3s-subshell. These minima occur at energies above the resonance-like peak that is due to the  $p \rightarrow d$  dipole transition that probes the  $l = 2$  potential barrier in Ar (cf. Fig. 4). In the two-photon ionization cross section, this minimum originates from a zero in the transition amplitude for the two-photon process  $3s \rightarrow \varepsilon_1 p \rightarrow \varepsilon_2 d$  at about  $\varepsilon_2 = 0.3 \text{ a.u.}$ , which can be seen in the two-photon partial cross section for the final-state  $\varepsilon_2 d(^1D)$  in Fig. 9(c). From Fig. 9(a) we see that this minimum in the two-photon amplitude from the Ar 3s-subshell also leads to a minimum in the generalized three-photon cross section from that subshell.

For the Xe atom, in order for the active electron to

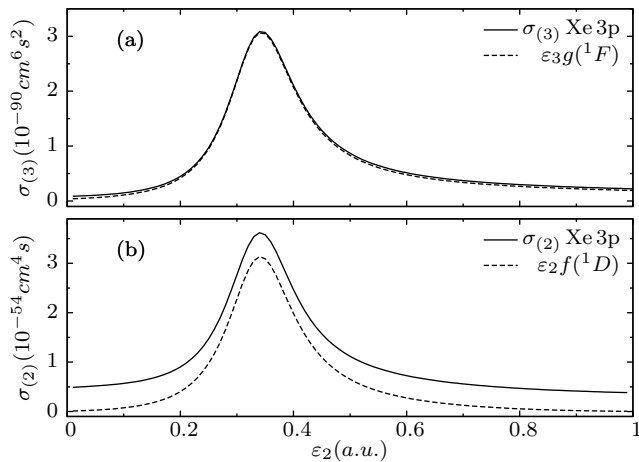


FIG. 10. (a): Generalized total cross section  $\sigma_{(3)}$  (solid line) for three-photon ionization of the Xe 3p-subshell and the partial cross section (dashed line) of the  $\epsilon_{3g}(^1F)$  channel. (b): Generalized total cross section  $\sigma_{(2)}$  (solid line) for two-photon ionization of the Xe 3p-subshell and the partial cross section (dashed line) of the  $\epsilon_{2f}(^1D)$  channel.

probe the  $f$  potential barrier (cf. Fig. 4) after it absorbs two photons, it should be ionized from a  $p$ -subshell. In Fig. 10, we plot both the three-photon and two-photon generalized cross sections for ionization from the Xe 3p-subshell. The shapes of the cross sections look quite similar to those shown in Fig. 5 when the first intermediate-state probes the  $f$  potential barrier. The peaks of the resonance-like shapes in the cross sections are located at the energy of the height of the  $f$  potential barrier,  $\epsilon_2 = 0.35$  a.u. Moreover, the dominant final-state channel in each case [i.e.,  $\epsilon_{3g}(^1F)$  in Fig. 10(a) and  $\epsilon_{2f}(^1D)$  in Fig. 10(b)] identifies the transition  $\epsilon_1 d \rightarrow \epsilon_2 f$  (cf. Fig. 2) as the one that produces the resonance-like shapes of the cross sections.

### C. Third (Final) State Potential Barrier Effects

In this section, we only consider final state potential barrier effects in three-photon ionization processes. Owing to electric dipole selection rules, the photoelectron must originate from an initial state having a parity that is opposite to that of the final state. For Kr and Ar, which have a  $d$  potential barrier, the initial state of the photoelectron must be a  $p$ -subshell in order to probe the  $d$  potential barrier after absorbing three photons. For Xe, which has an  $f$  potential barrier, the initial state of the photoelectron must be either an  $s$ -subshell or a  $d$ -subshell in order to probe the  $f$  potential barrier after absorbing three photons. We illustrate these potential barrier effects by examining the three-photon ionization of the 2p and 3p subshells of Kr and Ar and the 3s-, 4s-, and 4d-subshells of Xe.

In Fig. 11 we present the generalized three-photon total cross sections for ionization of the 2p- and 3p-subshells

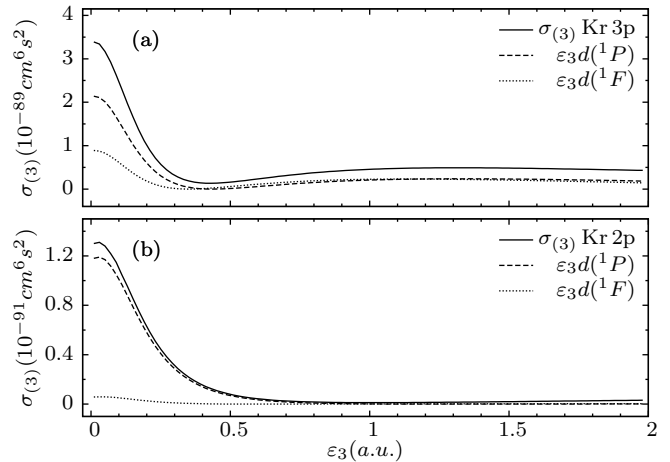


FIG. 11. Generalized total cross section  $\sigma_{(3)}$  (solid lines), and partial cross sections (dashed lines) for three-photon ionization from (a) the Kr 3p-subshell, and (b) the Kr 2p-subshell.  $\epsilon_3 \equiv \epsilon_{np} + 3\omega$ , where  $\epsilon_{np}$  is the  $np$ -orbital energy.

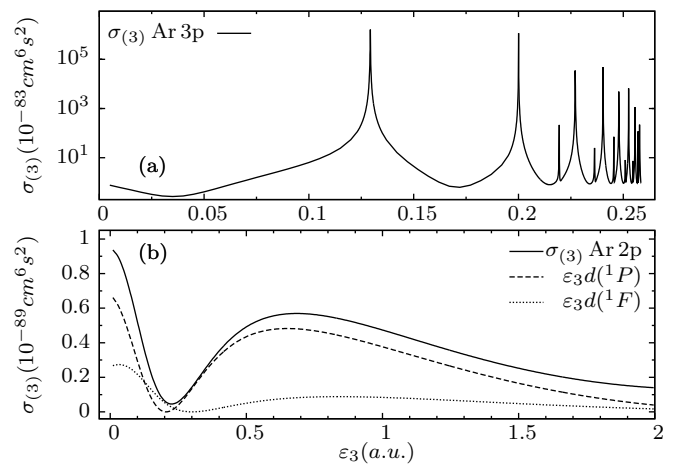


FIG. 12. Generalized total cross section  $\sigma_{(3)}$  (solid lines), and partial cross sections (dashed lines) for three-photon ionization of (a) Ar 3p, and (b) Ar 2p.  $\epsilon_3 \equiv \epsilon_{np} + 3\omega$ , where  $\epsilon_{np}$  is the  $np$ -orbital energy.

of Kr. Each cross section has a resonance very near its threshold, due to the low height of the  $d$  potential barrier for Kr (cf. Fig. 4). In both cases the contribution of the  $\epsilon_{3d}(^1P)$  channel is the largest in the resonance region. However, the branching ratios of the  $\epsilon_{3d}(^1P)$  and  $\epsilon_{3d}(^1F)$  channel partial cross sections are different for ionization from the 2p- and 3p-subshells.

In Fig. 12 we present the generalized three-photon total cross sections for ionization of the 2p- and 3p-subshells of Ar. As in the case of Kr, each cross section has a resonance very near its threshold, due to the low height of the  $d$  potential barrier for Ar (cf. Fig. 4). However, the three-photon generalized total cross section for ionization from the Ar 3p-subshell [Fig. 12(a)] is completely dominated by the Rydberg resonances and their large peak cross sections. Because the Ar 3p-subshell has a small

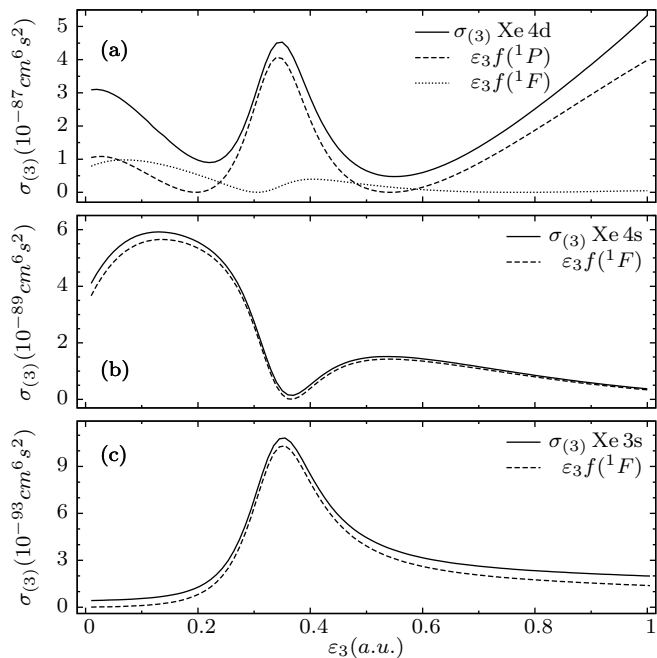


FIG. 13. Generalized total cross section  $\sigma_{(3)}$  (solid lines), and partial cross sections (dashed lines) for three-photon ionization of (a) the Xe 4d-subshell, (b) the Xe 4s-subshell, and (c) the Xe 3s-subshell.  $\varepsilon_3 \equiv \varepsilon_{nl} + 3\omega$ , where  $\varepsilon_{nl}$  is the  $nl$ -orbital energy for  $nl = 4d, 4s,$  and  $3s$ .

binding energy ( $0.53 a.u.$  in our model potential calculation), the first and second intermediate state wave packets of the photoelectron probe the Rydberg level energy region during three-photon ionization to the continuum. As shown in Fig. 12(b), Rydberg resonances do not have a significant influence on the three-photon cross section for ionization from the Ar  $2p$ -subshell, which is much more deeply bound. The latter cross section, however, exhibits a minimum near  $\varepsilon_3 = 0.2 a.u.$ , due to a zero in the  $\varepsilon_3 d(1P)$  transition amplitude. (Note that at a slightly higher energy, the  $\varepsilon_3 d(1F)$  transition amplitude also has a zero.) As in the case of Kr (cf. Fig. 11), the  $\varepsilon_3 d(1P)$  final-state channel gives the largest contribution to the total cross section.

In Fig. 13, we present the generalized three-photon total cross sections for ionization from the Xe  $4d$ -,  $4s$ -, and  $3s$ -subshells. Local maxima appear in the total cross sections for ionization from the  $4d$ - and  $3s$ -subshells at  $\varepsilon_3 = 0.35 a.u.$ , which is the height of the Xe potential barrier (cf. Fig. 4). For the case of the  $4s$ -subshell, however, a minimum occurs slightly above  $\varepsilon_3 = 0.35 a.u.$  due to a zero in the dominant  $\varepsilon_3 f(1F)$  final-state channel. In all cases shown, the  $\varepsilon_3 f$  channels are responsible for the resonance-like shapes, as expected.

#### D. Occurrence of Cooper Minima (CM)

We have seen in Secs. III B and III C above that CM do occur in the generalized cross sections for two- and three-photon ionization processes. However, the empirical rules for their occurrence in the case of one-photon ionization processes (cf., e.g., Refs. [44, 45]) do not apply in the case of multiphoton ionization. Thus, for example, CM never occur in one-photon ionization if the initial radial wave function has no node. However, as shown in Fig. 12(b) there is a Cooper minimum in the case of three-photon ionization of the Ar  $2p$ -subshell despite the fact that the  $2p$  radial wave function has no node. Also, in one-photon ionization CM only occur in transition amplitudes involving angular momentum transitions  $l \rightarrow l + 1$ ; they do not occur in those for  $l \rightarrow l - 1$  transitions. In the two- or three-photon ionization processes that are the focus of this paper, however, the change of orbital angular momentum of the photoelectron between its initial and final state can be any number from zero to two or three. Also, whereas in one-photon transitions, electric dipole selection rules limit the number of channels to at most two, in multiphoton transitions there are typically many channels (cf. Figs 1 – 3), of which more than one may have a transition amplitude that has a zero. For these reasons, the rules for the occurrence of CM in one-photon ionization processes do not apply to multiphoton ionization processes. To illustrate these remarks, in what follows we analyze the transition amplitudes for the three-photon generalized cross sections for ionization of the Xe  $4s$ - and  $4d$ -subshells (cf. Fig. 13).

Consider first three-photon ionization from the Xe  $4s$ -subshell. As shown in Fig. 1, multiphoton ionization from an  $s$ -subshell has fewer channels than from subshells with higher orbital angular momentum. For the Xe  $4s$ -subshell, there are two channels to the  $\varepsilon_3 p(1P)$  final state and only one channel to the  $\varepsilon_3 f(1F)$  final state. In Fig. 13(b), a Cooper minimum occurs at about  $\varepsilon_3 = 0.37 a.u.$  and ionization to the  $\varepsilon_3 f(1F)$  final state dominates the total cross section. In Fig. 14, we plot the transition amplitude for three-photon ionization from the Xe  $4s$  subshell to the  $\varepsilon_3 f(1F)$  final state, which clearly shows a zero at about  $\varepsilon_3 = 0.37 a.u.$  as does the radial integral for the  $s \rightarrow p \rightarrow d \rightarrow f$  transitions leading to it. The transition amplitude and the radial integral are related according to Eq. (10b). In this example, the minimum in the total cross section is exclusively determined by a vanishing radial integral associated with a single channel.

Three-photon ionization from the Xe  $4d$ -subshell has two CM in the total cross section [cf. Fig. 13(a)]. As shown in Fig. 3, three-photon ionization from a  $d$ -subshell may have seventeen channels leading to five different final states. However, as shown in Fig. 13(a), ionization to the  $\varepsilon_3 f(1P)$  final state is dominant, and its transition amplitude indeed vanishes twice, at  $\varepsilon_3 = 0.2 a.u.$  and  $0.55 a.u.$ , as shown in Fig. 15. From Fig. 3, one sees that the  $\varepsilon_3 f(1P)$  final state has five channels leading to it; however, these five channels involve (in our

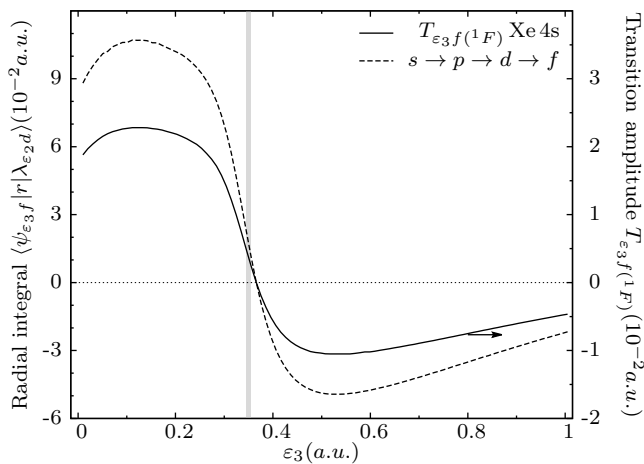


FIG. 14. The transition amplitude  $T_{\varepsilon_3 f(1F)}$  (solid line, with values on the right vertical axis, as indicated by the arrow) for three-photon ionization from the Xe 4s-subshell, and the corresponding radial integral (dashed line, with values on the left vertical axis) associated with the  $s \rightarrow p \rightarrow d \rightarrow f$  transitions of the photoelectron [cf. Eq. (10b)]. The vertical gray line indicates the energy of the Xe  $f$  potential barrier.

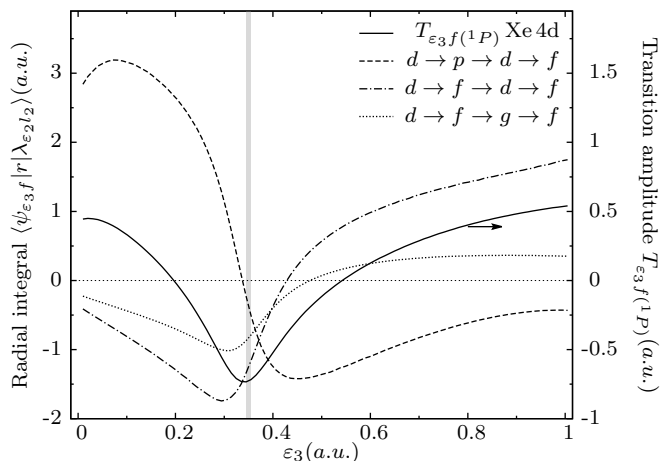


FIG. 15. The transition amplitude  $T_{\varepsilon_3 f(1P)}$  (solid line, with values on the right vertical axis, as indicated by the arrow) for three-photon ionization from the Xe 4d-subshell, and the three corresponding radial integrals (dashed lines, with values on the left vertical axis) associated with  $l_0 \rightarrow l_1 \rightarrow l_2 \rightarrow l_3$  transitions of the photoelectron [cf. Eq. (10b)]. The vertical gray line indicates the energy of the Xe  $f$  potential barrier.

single active electron model) only three different radial integrals that depend on the sequence of angular momentum transitions of the photoelectron, as indicated in Fig. 15. Each of these radial integrals is seen to vanish somewhere near the energy of the Xe  $f$  potential barrier height,  $0.35 a.u.$  Although each radial integral has only one zero, their interference results in two zeros in the transition amplitude and thus causes two CM in the total cross section. Clearly, CM in multiphoton ionization processes are more complicated to analyze than for

one-photon ionization processes.

#### IV. SUMMARY AND CONCLUSIONS

In conclusion, we have investigated three-photon ionization from various subshells of Ar, Kr, and Xe in which the photoelectron wave packet after absorbing one-, two-, or three-photons probes the  $d$  potential barriers in Ar and Kr and the  $f$  potential barrier in Xe. In those cases in which the photoelectron wave packet probes the potential barrier after absorbing one- or two-photons, we have compared the generalized three-photon ionization cross sections with the corresponding generalized two-photon ionization cross sections from the same subshells and have found great similarity in the corresponding results. These results indicate that potential barrier effects are general features of multiphoton ionization processes for any atoms and ions having an effective potential barrier. The clearest resonance-like features occur in multiphoton ionization of inner subshell electrons, for which the photon energies are large. For multiphoton ionization of valence-shell electrons, which have small binding energies, the resonance-like features due to potential barriers can be overshadowed by intermediate-state Rydberg resonances.

The empirical rules for the occurrence of Cooper minima in one-photon ionization processes are found not to apply for multiphoton ionization. In essence, the larger the number of photons, the greater the number of alternative channels to reach a given final state. We have demonstrated that in cases in which one channel is dominant, one or more zeros in its radial matrix elements can be observed in the total multiphoton cross section. However, formulation of general rules for when such zeros occur would require a systematic set of investigations for a large range of atoms, which is beyond the scope of this paper.

Experimental observation of the potential barrier effects predicted here in multiphoton ionization processes will require tunable XUV wavelengths. A recent experiment [38] for single ionization of an electron from the Xe 4d-subshell using 93 eV photons found that the electron signal depended quadratically on the XUV pulse energy, indicating thus a two-photon ionization process. An R-matrix Floquet simulation in the same Ref. [38] provides evidence that the  $4d \rightarrow f$  giant dipole resonance, well-known in single photon ionization of the Xe 4d-subshell, affects the two-photon cross section. Confirmation of this finding will require two-photon ionization cross sections as a function of photon energy.

Finally, we note that our use of the single-active-electron model to describe multiphoton ionization cross sections limits the quantitative accuracy of our predictions. Electron correlations will quantitatively change the magnitude and the position of the resonance-like potential barrier effects on multiphoton cross sections as well as the shape and location of any Cooper minima.

Qualitatively, however, the resonance-like potential barrier effects (including giant dipole resonances) have been shown in this paper to be such prominent features of multiphoton ionization processes that their observation experimentally is unquestionable. Our results in this paper may thus serve as a qualitative guide for future tunable XUV measurements of multiphoton ionization cross sections.

## ACKNOWLEDGMENTS

This work is supported in part by DOE, Office of Science, Division of Chemical Sciences, Geosciences, and Biosciences, under Grant No. DE-FG03-96ER14646.

## Appendix: Angular Integrals

In this appendix we provide expressions for the angular factors in Eq. (10), denoted by  $A_2$  and  $A_3$  respectively for two- and three-photon ionization from a closed-shell atom interacting with a linearly-polarized laser field. Consider first three-photon ionization processes, for which the angular factor  $A_3$  must be calculated for each allowed transition channel, denoted schematically by

$$\begin{aligned} n_0 l_0^q(L_0 S_0) &\xrightarrow{+\gamma} n_0 l_0^{q-1}(\tilde{L}\tilde{S})\varepsilon_1 l_1(L_1 S_1) \\ &\xrightarrow{+\gamma} n_0 l_0^{q-1}(\tilde{L}\tilde{S})\varepsilon_2 l_2(L_2 S_2) \\ &\xrightarrow{+\gamma} n_0 l_0^{q-1}(\tilde{L}\tilde{S})\varepsilon_3 l_3(L_3 S_3), \end{aligned} \quad (\text{A.1})$$

where the arrows denote the absorption of a photon  $\gamma$ ,  $\varepsilon_N$  and  $l_N$  are the energy and orbital angular momen-

tum of the photoelectron,  $\tilde{L}$  and  $\tilde{S}$  refer to the ionic term level,  $L_N$  and  $S_N$  are the total orbital and spin angular momenta of the ion-photoelectron system, and  $q$  is the number of electrons in the initial subshell. We have suppressed, for simplicity, explicit notation of any magnetic quantum numbers needed to be summed over when calculating angular factors. The ionization channel notation (A.1) may be used also for two-photon ionization processes if we treat the second state  $\varepsilon_2 l_2(L_2 S_2)$  as the final state. For a closed-shell atom, our evaluation of the angular factors is simplified due to the fact that  $q = 4l_0 + 2$ ,  $L_0 = 0$ ,  $S_0 = 0$ , therefore,  $L_1 = 1$ ,  $S_N = 0$  according to angular momentum conservation, and there is only one allowed ionic term level,  $\tilde{L} = l_0$  and  $\tilde{S} = \frac{1}{2}$ . We have evaluated the angular factors for two- and three-photon ionization following the procedures in Ref. [54] to obtain

$$\begin{aligned} A_2 = & - [l_1] ([l_0][l_2][L_2])^{\frac{1}{2}} \begin{Bmatrix} 1 & l_2 & l_1 \\ l_0 & 1 & L_2 \end{Bmatrix} \\ & \times \begin{pmatrix} l_2 & 1 & l_1 \\ 0 & 0 & 0 \end{pmatrix} \begin{pmatrix} l_1 & 1 & l_0 \\ 0 & 0 & 0 \end{pmatrix} \begin{pmatrix} 1 & L_2 & 1 \\ 0 & 0 & 0 \end{pmatrix}, \end{aligned} \quad (\text{A.2})$$

$$\begin{aligned} A_3 = & (-1)^{l_1} [l_1][l_2][L_2] (2[l_0][l_3][L_3])^{\frac{1}{2}} \begin{Bmatrix} 1 & l_2 & l_1 \\ l_0 & 1 & L_2 \end{Bmatrix} \\ & \times \begin{pmatrix} l_2 & 1 & l_1 \\ 0 & 0 & 0 \end{pmatrix} \begin{pmatrix} l_1 & 1 & l_0 \\ 0 & 0 & 0 \end{pmatrix} \begin{pmatrix} 1 & L_2 & 1 \\ 0 & 0 & 0 \end{pmatrix} \\ & \times \begin{pmatrix} l_3 & 1 & l_2 \\ 0 & 0 & 0 \end{pmatrix} \begin{pmatrix} L_2 & L_3 & 1 \\ 0 & 0 & 0 \end{pmatrix} \begin{Bmatrix} 1 & l_3 & l_2 \\ l_0 & L_2 & L_3 \end{Bmatrix}, \end{aligned} \quad (\text{A.3})$$

where the  $[X] \equiv 2X + 1$  and the symbols  $\{X\}$  and  $(X)$  are respectively the Wigner  $6j$ - and  $3j$ -symbols. The result for two-photon ionization in Eq. (A.2) agrees with those in Refs. [31, 32]. Note that our results for three-photon ionization of atomic hydrogen in its ground state (cf. Table II) employ  $A_3$  in Eq. (A.3) divided by  $\sqrt{2}$ , because hydrogen has only one electron in its  $1s$ -subshell.

- 
- [1] J. Feldhaus and B. Sonntag, "Free-Electron Lasers - High-Intensity X-Ray Sources," in *Strong Field Laser Physics*, edited by T. Brabec (Springer, New York, 2008) pp. 91–107.
- [2] J. Ullrich, A. Rudenko, and R. Moshhammer, *Annu. Rev. Phys. Chem.* **63**, 635 (2012).
- [3] P. Lambropoulos and G. M. Nikolopoulos, *Eur. Phys. J. Special Topics* **222**, 2067 (2013).
- [4] W. Ackermann *et al.*, *Nature Photon.* **1**, 336 (2007).
- [5] K. Tiedtke *et al.*, *New J. Phys.* **11**, 023029 (2009).
- [6] H. Chapman, J. Ullrich, and J. M. Rost, *J. Phys. B* **43**, 190201 (2010).
- [7] J. Feldhaus, *J. Phys. B* **43**, 194002 (2010).
- [8] T. Shintake *et al.*, *Nature Photon.* **2**, 555 (2008).
- [9] P. Emma, *Nature Photon.* **4**, 641 (2010).
- [10] P. H. Bucksbaum, R. Coffee, and N. Berrah, *Adv. At. Mol. Opt. Phys.* **60**, 239 (2011).
- [11] B. D. Patterson *et al.*, *New J. Phys.* **12**, 035012 (2010).
- [12] G. Geloni, E. Saldin, L. Samoylova, E. Schneidmiller, H. Sinn, T. Tschentscher, and M. Yurkov, *New J. Phys.* **12**, 035021 (2010).
- [13] T. Ishikawa *et al.*, *Nature Photon.* **6**, 540544 (2012).
- [14] A. Rudenko, Y. Jiang, M. Kurka, K. U. Kühnel, L. Foucar, O. Herrwerth, M. Lezius, M. F. Kling, C. D. Schröter, R. Moshhammer, and J. Ullrich, *J. Phys. B* **43**, 194004 (2010).
- [15] M. Richter, S. V. Bobashev, A. A. Sorokin, and K. Tiedtke, *J. Phys. B* **43**, 194005 (2010).
- [16] K. Tamasaku *et al.*, *Nature Photon.* **8**, 313316 (2014).
- [17] T. Inada *et al.*, *Phys. Lett. B* **732**, 356359 (2014).
- [18] S. Shwartz *et al.*, *Phys. Rev. Lett.* **112**, 163901 (2014).
- [19] U. Fano and J. W. Cooper, *Rev. Mod. Phys.* **40**, 441 (1968).
- [20] M. Amusia and N. A. Cherepkov, *Case Stud. At. Phys.* **5**, 47 (1975).
- [21] A. F. Starace, in *Handbuch der Physik*, Vol. 31, edited by W. Mehlhorn (Springer-Verlag, Berlin, 1982) pp. 1–121.

- [22] M. S. Pindzola and H. P. Kelly, Phys. Rev. A **11**, 1543 (1975).
- [23] R. Moccia, N. K. Rahman, and A. Rizzo, J. Phys. B **16**, 2737 (1983).
- [24] A. L’Huillier, L. Jönsson, and G. Wendin, Phys. Rev. A **33**, 3938 (1986).
- [25] A. F. Starace and T.-F. Jiang, Phys. Rev. A **36**, 1705 (1987).
- [26] A. L’Huillier and G. Wendin, J. Phys. B **20**, L37 (1987).
- [27] A. L’Huillier and G. Wendin, Phys. Rev. A **36**, 4747 (1987).
- [28] A. L’Huillier and G. Wendin, J. Phys. B **21**, L247 (1988).
- [29] T.-F. Jiang and A. F. Starace, Phys. Rev. A **38**, 2347 (1988).
- [30] A. L’Huillier, X. Tang, and P. Lambropoulos, Phys. Rev. A **39**, 1112 (1989).
- [31] C. Pan, B. Gao, and A. F. Starace, Phys. Rev. A **41**, 6271 (1990).
- [32] C. Pan and A. F. Starace, Phys. Rev. A **44**, 324 (1991).
- [33] F. Robicheaux and B. Gao, Phys. Rev. A **47**, 2904 (1993).
- [34] H. W. van der Hart, Phys. Rev. Lett. **95**, 153001 (2005).
- [35] H. W. van der Hart, Phys. Rev. A **73**, 023417 (2006).
- [36] L. Hamonou, M. A. Lysaght, and H. W. van der Hart, J. Phys. B **41**, 121001 (2008).
- [37] L. Hamonou and H. W. van der Hart, J. Phys. B **43**, 045601 (2010).
- [38] V. Richardson, J. T. Costello, D. Cubaynes, S. Düsterer, J. Feldhaus, H. W. van der Hart, P. Juranić, W. B. Li, M. Meyer, M. Richter, A. A. Sorokin, and K. Tiedke, Phys. Rev. Lett. **105**, 013001 (2010).
- [39] M. Amusia and J.-P. Connerade, Rep. Prog. Phys. **63**, 41 (2000).
- [40] R. W. Ditchburn, J. Tunstead, and J. G. Yates, Proc. R. Soc. Lond. A **181**, 386 (1943).
- [41] D. R. Bates, Proc. R. Soc. Lond. A **188**, 350 (1947).
- [42] M. J. Seaton, Proc. R. Soc. Lond. A **208**, 418 (1951).
- [43] J. W. Cooper, Phys. Rev. **128**, 681 (1962).
- [44] S. T. Manson, Phys. Rev. A **31**, 3698 (1985).
- [45] R. Y. Yin and R. H. Pratt, Phys. Rev. A **35**, 1149 (1987).
- [46] L.-W. Pi and A. F. Starace, Phys. Rev. A **82**, 053414 (2010).
- [47] P. Lambropoulos, Adv. At. Mol. Phys. **12**, 87 (1976).
- [48] A. Dalgarno and J. T. Lewis, Proc. Roy. Soc. Lond. A **233**, 70 (1955).
- [49] F. Herman and S. Skillman, *Atomic Structure Calculations* (Prentice Hall, Englewood Cliffs, NJ, 1963).
- [50] M. Aymar and M. Crance, J. Phys. B **14**, 3585 (1981).
- [51] M. Marinescu, H. R. Sadeghpour, and A. Dalgarno, J. Opt. Soc. Am. B **10**, 988 (1993).
- [52] B. Gao and A. F. Starace, Comput. Phys. **1**, 70 (1987).
- [53] A. P. Yutsis, I. B. Levinson, and V. V. Vanagas, *Mathematical Apparatus of the Theory of Angular Momentum* (Israel Program for Scientific Translations, Jerusalem, 1962).
- [54] J. S. Briggs, Rev. Mod. Phys. **43**, 189 (1971).
- [55] E. Balcar and S. W. Lovesey, *Introduction to the Graphical Theory of Angular Momentum: Case Studies* (Springer, Berlin Heidelberg, 2009).
- [56] E. Karule, J. Phys. B **21**, 1997 (1988).
- [57] B. Gao and A. F. Starace, Phys. Rev. Lett. **61**, 404 (1988).
- [58] E. Karule and A. Gailitis, J. Phys. B **43**, 065601 (2010).